This is a repository copy of *Deciphering the mechanisms of bacterial inactivation on HiPIMS sputtered CuxO-FeOx-PET surfaces : from light absorption to catalytic bacterial death*.

White Rose Research Online URL for this paper:
https://eprints.whiterose.ac.uk/187328/

Version: Accepted Version

eprints@whiterose.ac.uk
https://eprints.whiterose.ac.uk/

Deciphering the mechanisms of bacterial inactivation of HiPIMS sputtered Cu_xO-FeO_x-PET surfaces: from light absorption to bacterial death

Arthur Graf[1], Jake Finkel[1], Adrien A. P. Chauvet[1]* and Sami Rtimi[2]*

[1] The University of Sheffield, Department of Chemistry, Dainton Building, C94, United Kingdom.

[2] Ecole Polytechnique Fédérale de Lausanne, EPFL-SB-ISIC-GPAO, Station 6, 1015 Lausanne, Switzerland.

The production of non-toxic, affordable and efficient antibacterial surfaces is key to the wellbeing of our societies. In this aim, antibacterial thin films have been prepared using earth-abundant metals deposited with a high-power impulse magnetron sputtering methods. All Fe, Cu and mixed FeCu oxides films shows high bacterial inactivation properties under exposure to indoor light (UVA-Visible, 340-720 nm). The photocatalytic mechanisms of these films were investigated, from the absorption of UV-Vis photons up to the bacteria's fate, by means of ultrafast transient spectroscopy, stop-flow cytometry and MDA quantification. The primary driving force leading to bacterial inactivation is found to be the oxidative stresses at the interface between the film and the organism. Such stresses are a direct consequence of the photo-generated electron-hole pairs in the

1

metallic layer. The structure and composition of the films was characterized by energy dispersive X-ray, X-ray photo electron and optical spectroscopy. While the composition and metal oxidation states are distinct in all three films, the difference in photocatalytic efficiency can, at first sight, be explained as direct consequence of their absorbance.

KEYWORDS: Antibacterial, thin film, sputtered Cu_xO-FeO_x-PET; photocatalysis; X-ray photoelectron, ultrafast spectroscopy, electron-hole pairs.

1. Introduction

Indoor surfaces are generally prone to incubate life-threatening pathogens. Whether we are looking at the infrastructure (floors, walls, shelves, etc.) or equipment (tools, cutleries, etc.), the ability to sterilize these surfaces is a key to human comfort and health. Healthcare-associated infections, in hospitals for example, are of prime concern; so much so that the United Nations (UN) made it as one of their Sustainable Development Goals [1], and the World Health Organization (WHO) made antimicrobial resistance one of their strategic priorities [2]. The number of patients that are affected by healthcare-associated infections is in the order of 10^8 each year, leading to significant mortality and financial losses for health services across the world [3-5]. In this aim, we propose to develop self-sterilizing surfaces. These surfaces represent an exceptional opportunity to reconsider approaches related to human health, including endemic, long-standing infectious diseases.

To date, surfaces of infrastructure, furniture and devices such as catheters for example, are sterilized by covering them with antiseptics, antibiotics or by using classical metal-based agents that are toxic to humans as well [6, 7]. These antibacterial agents have shown a lack of stability, little adherence or non-thermal resistance to tissues and other polymer surfaces. Additionally, they

2

show progressive loss of their intrinsic antibacterial properties over short times-scales, which hinder their use in hospital facilities and in public places [4].

In this work we report the preparation and investigation of ultra-thin antibacterial films prepared by direct current magnetron sputtering (DCMS) and high power impulse magnetron sputtering (HiPIMS) [5, 8, 9]. In comparison to the current sterilizing methods (previously mentioned) these films are flexible and mechanically stable, which make them adequate to a wide range of application in hospital and other facilities. Sputtered nano-thin films are particularly promising since they show high adhesion to the substrate and are uniform. They also demonstrate fast antibacterial properties while being drug resistant. Furthermore, HiPIMS-prepared films have a more compact surface and are resistant to oxidation and corrosion [10, 11]. Finally, the possibility to nano-structure HIPIMS films provides with an enhanced interaction between the material and the bacteria at the interface, thus enhancing their inactivation efficiency [12-14].

The films under investigation are made of iron and copper oxides; both being non-toxic and earth-abundant elements. Iron oxide (FeO_x) coatings on different substrates from colloidal precursors have been reported as a photocatalyst to degrade pollutants and/or to inactivate bacteria via photo-Fenton processes [15-19]. The degradation of pollutants on Fe-supported on polyethylene (PET)-maleic anhydride films, and on Fe-sulfonic Nafion exchange membranes have been already reported in the past decade [19-22]. Similarly, copper oxides (Cu_xO) have been reported to exhibit antibacterial properties via cell wall disruption and/or disrupting the cell metabolism [23, 24]. The sterilizing properties of Cu_xO and Cu-ions deposited on polymer and textiles in the dark or under light have been recently reported [11, 25, 26]. Cu_xO was also shown to produce highly oxidative radicals under light illumination leading to bacterial inactivation via surface contact effects [19, 27].

In this study, we present novel FeO_x and Cu_xO antibacterial thin-films that are prepared using the HiPIMS deposition technique on polyethylene substrate. We report on their composition, structure and electronic properties. The antibacterial properties and physiological states of bacteria on the sputtered thin films are demonstrated via different strains of *E. coli*. The nanostructure of the sputtered layer is characterized by diffuse reflectance spectroscopy (DRS), X-ray photoelectron spectroscopy (XPS) and transmission electron microscopy (TEM). The electronic properties and early electron dynamics are investigated by means of ultrafast laser spectroscopy.

2. Experimental Section

2.1. Materials preparation

The Cu_xO, FeO_x and FeO_x-Cu_xO thin films were sputtered using reactive sputtering process. Fe and Cu targets were purchased from Lesker (purity 99.99%). The sputtering chamber was operated at a high vacuum with a residual pressure of 3.2 x 10^{-5} Pa. The stainless-steel vacuum chamber is equipped with two confocal (off axis, 25.6°) targets of 5 cm in diameter. A HiP3 5KW Solvix generator was used for the HiPIMS deposition of Cu_xO and was operated at an average power of 100 W (5 W.cm^{-2}) with a pulse-width of 50 μs and a frequency of 1 kHz. To dissipate the high current at the Cu-target surface, a spacer was placed under the target. The FeO_x was deposed using DC-mode as previously reported [28]. This choice is based on two reasons: (i) the deposition of FeO_x was reported to operate without ions release, and (ii) the deposition of Cu_xO using HiPIMS was seen to reduce the release of cytotoxic Cu-ions [27]. The distance target-to-sample was fixed at 10 cm in order to obtain homogeneous distribution of the sputtered films. The sample holder was rotating at a speed of 18 rpm. The magnetic field caused by the magnets behind the Fe-target in a magnetron sputtering setting cannot go out onto the surface target due to its para-magnetization

[28]. This hinders the formation of the plasma and thus inhibit the Fe-deposition. In order to address this challenge, the target was machined in order to let the magnetic field pass through the target as shown in Figure 1. This geometry forces the electrons to follow the normal hopping trajectory along the target.
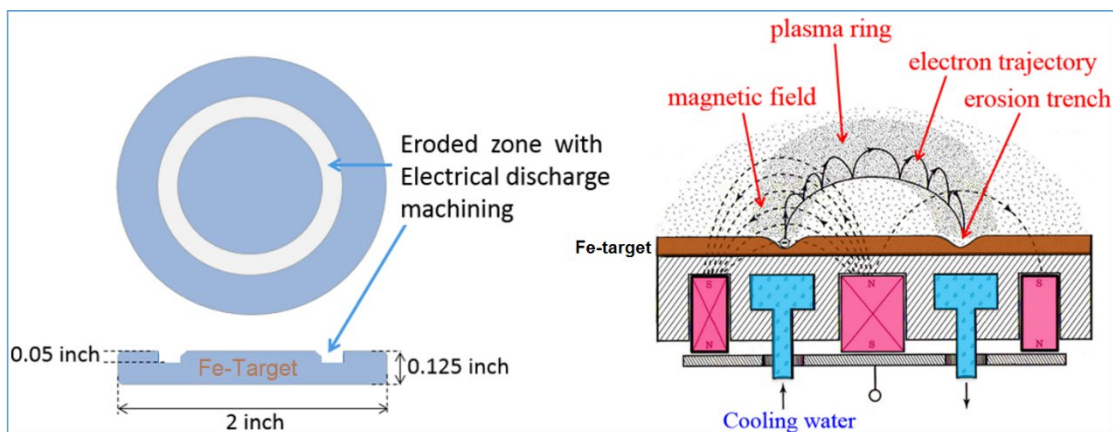
Figure 1: Iron target artificially modified allowing DCMS FeO$_x$ deposition (Reproduced from App. Catal. B: Environm, 213 (2017) 62-73 under the Elsevier-licence number 4565220956723) [29].

2.2. Bacterial inactivation, bacterial cell-wall lysis and flow cytometry tests

In order to test the antibacterial activity of the co-sputtered samples, *E. coli* K12 strain was obtained from the Deutsche Sammlung von Mikroorganismen und Zellkulturen GmbH (DSMZ) ATCC23716, Braunschweig, Germany. The *E. coli* K12 organisms were master-plated and incubated overnight in tryptic broth at 37ºC. Overnight cultures of *E. coli* were washed twice in 0.9% NaCl and lately diluted to the pre-selected concentration. The sputtered PE fabrics were sterilized by incubating them at 80°C for 3h. The 50 µL culture aliquots with an initial

concentration of ~ 5.8×10^6 CFU mL^{-1} in NaCl/KCl (pH 7.2) were placed on coated and uncoated (control) PE fabrics of 4 cm^2. Samples were then placed on Petri dishes provided with a lid to prevent evaporation. After each bacterial determination, the fabric was transferred into a sterile 2 mL Eppendorf tube containing 950 µL autoclaved NaCl/KCl saline solution. This solution was subsequently mixed thoroughly using a Vortex. Serial dilutions were made in NaCl/KCl solution. A 100-µL aliquot was pipetted onto a nutrient agar plate and then spread over the surface of the plate using standard plate method. Agar plates were incubated lid down, at 37°C for 24h before colonies were counted. Three independent assays were done for each sputtered (and control) sample. To verify that no re-growth of *E. coli* occurs after the first bacterial inactivation cycle, the sputtered fabrics were kept in the saline solution for 24 hours at 37°C. Then, the bacterial suspension of 100 µL was deposited on three Petri dishes to obtain replicates. The samples were incubated at 37°C for 24 h. No bacterial re-growth was observed after their inactivation on the sputtered samples.

The mutant *E. coli* strain deficient in porins (OmpF and OmpC porins) were prepared as described in our previous study [11, 27]. This approach allowed to separate the bacterial inactivation kinetics induced by the ions release that can penetrate the cells (i) the Cu-ions able to penetrate inside the cell or the oxidation of the cell wall (from now as: surface-contact). The *E. coli K12* ATCC bacterial strain is isogenic with the TK 821 genetically modified porinless bacteria. Both bacteria contain genotypes that reproduce indefinitely and remain similar for many generations. The same culture conditions are used for both the normal *E. coli* and the genetically modified *E. coli* were to ensure identical growth of both strains.

In order to elucidate whether the photocatalytic bacterial oxidation happens at the interface with the coatings (external attack) or through ions that penetrate inside the cells (internal attack) to

inactivate them from inside, the bacterial cell peroxidation was evaluated on normal and genetically modified (porinless) *E. coli*. During external attack, the lipid peroxidation leads to the generation of malondialdehyde (MDA). The formation of MDA was measured by mean of a high-performance liquid chromatography (HPLC, Agilent 1100 series) equipped with a UV absorbance detector. The bacterial suspensions after the illumination on the sputtered samples were filtered (to remove the bacterial debris and alive cells) and injected via auto-sampler. The samples were eluted at a flow rate of 0.9 ml/min through a Nucleosil C18 (Marcherey-Nagel) column using a mobile phase consisted of a 3 mM KH_2PO_4-MeOH (65-35 v/v%) solution. The MDA chromatogram peaks were monitored at 268 nm wavelength and a retention time of MDA was 3.9 min [18].

An acoustic-focusing ThermoFisher Attune NxT flow cytometer was used to elucidate the physiological states of the bacterial cells on the sputtered samples. It is provided with a 4-laser and 14-detector instrument allowing a large variability in laser excitation and permitting to the cells to be perfectly lined up and to cross the lasers at their focal point.

All the sputtered samples reported in this study were irradiated using Osram Lumilux 840 actinic lamps system (similar to the ones used in hospitals). The light source emits a light dose of 5 mW/cm^2 from 340 to 720 nm. The ions release from the sputtered surfaces were quantified by inductively coupled-plasma mass spectrometry.

2.3. Atomic composition and structure

In order to visualize the microstructure of the films, the coated PE fabrics were embedded in epoxy polymer then cut with ultra-microtome into 80-100 nm thick layers. Because of the soft and flexible nature of the polyethylene substrate, different embedding media were tested. Two pieces

from the same sample were glued together as a sandwich, without extra embedding and were cut using a cryo-ultra-microtome sectioning at temperature –140 °C (Ultramicrotome: Leica EM UC7). These layers were placed on TEM carbon grid. FEI Tecnai Osiris microscope was used for imaging and operated at 200 kV, with spot size of 5, dwell time 50 μs and real time 600 s. Chemical analysis was performed using an EDX system.

The atomic structure of the films was determined by XPS analysis. These were carried out on a Kratos Supra instrument with a monochromated aluminium source. The composition of each sample is investigated at two different locations of area 700 by 300 µm. Survey scans were collected between 1200 to 0 eV binding energy, at 160 eV pass energy, 1 eV intervals, and one 300 second sweep across the energy range. High-resolution O 1s, N 1s and C 1s XPS spectra were also collected at 20 eV pass energy and 0.1 eV intervals for each analysis point over an appropriate energy range, with one 300 second sweep for carbon and oxygen and two sweeps for nitrogen. The XPS fitting were realized using Advantage Analysis software from Thermo Scientific. For the elements that are subjected to spin-orbit coupling (i.e Metals, or any other where the ejected electron is different from an s-orbital electron, since the l quantum number is different than 0), the most intense peak is taken as the reference and assumed to correspond to the $p3/2$ states, unless specified otherwise. The final adjustments on the curves were made using OriginPro 8.0.

2.3. Ultrafast transient absorption spectroscopy

The spectroscopy was performed using a Helios module seeded by a Spitfire Ace - PA 40 [30]. The output pulses were centered around 800 nm with a 60 fs FWHM and a 10 kHz repetition rate. This train of pulses were divided into pump and probe. While the pump pulses were passed onto a BBO for frequency doubling, resulting in an ~400 nm excitation, thus exciting well above the

bandgap of the samples, the probe was passed onto a Sapphire crystal to generate a white light continuum. The copper oxide film was analyzed using pulses of 1 mW whilst the iron and mixed copper-iron films were analyzed using pulses of 3.5 mW. The data were acquired using the provided Helios software and analyzed by means of Singular Value Decomposition using Glotaran and Fourier analysis using Matlab.

3. Results and discussions

3.1. Bacterial inactivation: efficiency and mechanisms

The antibacterial properties of the Cu-PET, Fe-PET and Cu-Fe-PET sputtered films are demonstrated in Figure 2 following the *E. coli* inactivation. While all three films efficiently inactivate *E. coli* in matters of hours, it is seen that the composite is two times faster than Cu_xO-PET and three times faster than FeO_x-PET; the reason of which will be discussed subsequently in light of their structure and mechanisms.
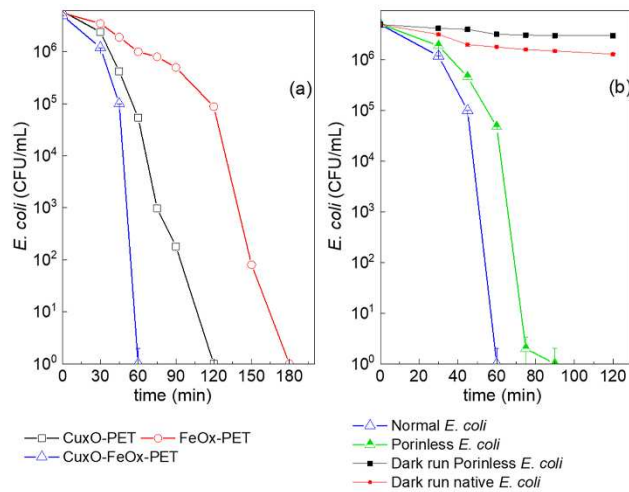
Figure 2: (a) Bacterial inactivation on Cu_xO, FeO_x and Cu_xO-FeO_x-PET under indoor actinic light (5 mW/cm2). (b) Antibacterial activity of normal E. coli and porinless E. coli under indoor

light on Cu$_x$O-FeO$_x$-PET: extracellular versus intracellular bacterial inactivation. Control experiment: dark run normal and porinless bacteria in the dark on Cu$_x$O-FeO$_x$-PET.

Similar results were reported for bacterial and fungi inactivation using Cu$_x$O sputtered surfaces [31]. In a separate study, *E. coli* inactivation was reported on FeO$_x$ sputtered surfaces and the action mechanism was attributed to the interfacial charge transfer between the different iron oxides presenting different band-gaps [28]. The same authors studied also the surface regeneration by the use of a 1M NaOH solution [28].

It is commonly agreed that bacterial inactivation on Cu$_x$O, FeO$_x$ and their combination involve photo-generated ions and oxygen radicals at the sputtered surfaces that enter in contact with the bacteria. Either these ions remain outside the bacteria's cells or penetrate the bacterial cell wall through the porins and alter the enzymatic balance and/or disturb the bacterial replication mechanisms. To differentiate between the intracellular or the extracellular bacterial inactivation mechanism, genetically modified bacterial without porins were used.

Figure 2b shows the bacterial inactivation of normal and genetically modified bacterial. In both light and dark conditions, the inactivation kinetics of normal and genetically modified bacteria are comparable. This result suggests that the ions and oxygen radicals mostly act outside the cell. These photoproducts thus have the potential to indiscriminately affect any living organisms that are in their vicinity. However, it is worth mentioning that the release from the sputtered surfaces is ionic and not particulates. As ions are less toxic than particulates, the observed ions-release reduces the possible cytotoxic effect for human cells because they can tolerate higher ionic concentration than bacterial cells [11, 12].

The quantification of the released ions from the sputtered surfaces was monitored by inductively coupled plasma mass spectrometry (ICP-MS). Fe- and/or Cu-released (µg/L) from the sputtered Cu_xO-FeO_x-PET sample were 4 ppb and 6 ppb, respectively. This is far the allowed toxicity levels fixed by the regulation for water and health [32, 33].
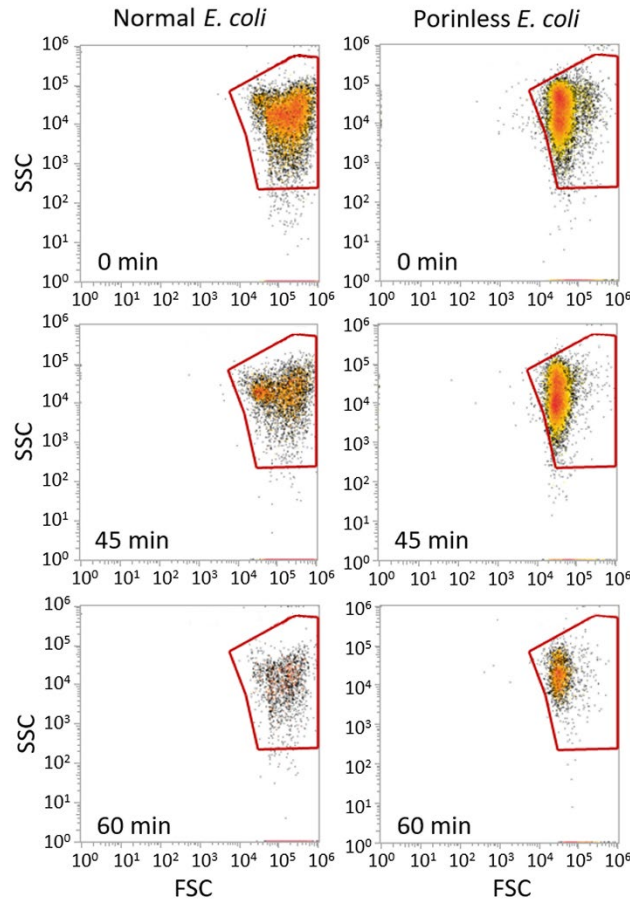
Figure 3: Cytometry and bacterial morphology changes during the photocatalytic oxidation on sputtered surfaces.

To better understand the bacterial action of Cu_xO-FeO_x-PET on the normal and porinless bacteria, flow cytometry was carried out during the bacterial inactivation period. Figure 3 shows that bacterial initial concentration exhibited quite similar physiological distribution of the

inoculum with a small shoulder (physiological state) for the normal bacteria. After 45 min irradiation, the normal bacteria cells were split to two distinct physiological states/families with respect to FSC-A values. However, the porinless bacteria show the same physiological trend compared to that of the alive bacteria. This suggests the presence of two distinct mechanisms for bacterial inactivation: a predominately external effect and a minor effect of ions (clearly seen after 45 min illumination of the bacteria on the Cu_xO-FeO_x-PET sample). The absence of this second family in the porinless bacteria reflects that the bacterial cells were inactivated mainly by a unique mechanism with the remaining cell debris being rapidly degraded. The little cells concentration observed after 60 min photocatalysis on the sputtered Cu_xO-FeO_x-PET, were quantified to be around 10^2 CFU/ml. This level coincides with the detection limit of the plate-count agar method and corresponds to the tolerable bacterial concentration in hospital settings [11, 28, 31]. The latter solution was cultivated on agar and incubated overnight at 37°C to check for proliferation of new bacterial colonies but none were subsequently formed. The lack of new colonies implies that the detected remaining cells by the flow cytometry are either strongly damaged or non-viable.

Bacteria are able to scavenge and preclude reactive oxygen species (ROS) by generating superoxide dismutase (SOD) and catalase (specific for the neutralization of H_2O_2) in their cytoplasm. The ROS deactivation pathway is known to be governed by four genes (katA, katE, katG and katX) that express different catalase [34]. The katE and katG are at the origin of the dominant catalase species as reported by Imlay [35]. The two *E. coli* strains used in this study were analyzed at the same growth phase. This is necessary due to the possible membrane permeability changes that can happen during the photocatalysis on the sputtered surfaces. The optical density values of both stains (bacterial suspensions) were observed to be similar indicating that the genetic

differences do not influence the cell growth and the observed bacterial inactivation differences were due to the oxidative stress generated at the interface of the sputtered films.
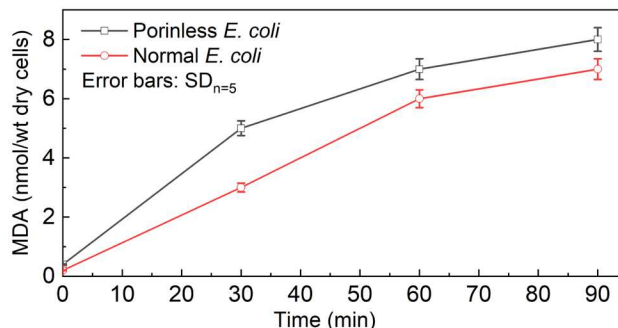
Figure 4: MDA detection from the membrane oxidation of both strains used in this study on Cu_xO-FeO_x films sputtered on PET.

Figure 4 shows the MDA quantification of both *E. coli* strains. It is readily seen that the difference of the MDA formation is 10-15%. This suggest that the strong oxidative stress happening on the interface of the sputtering Cu_xO-FeO_x-PET is one of the driving forces leading to bacterial inactivation. The contribution of ions that can penetrate inside the cells is seen to be minimal. This can be concomitant with pH values at the interface between bacteria and the sputtered films.

3.1. Film composition and structure

3.2.1. XPS analysis

The XPS survey spectra shown in Figure 5 illustrates the atomic composition of each film.
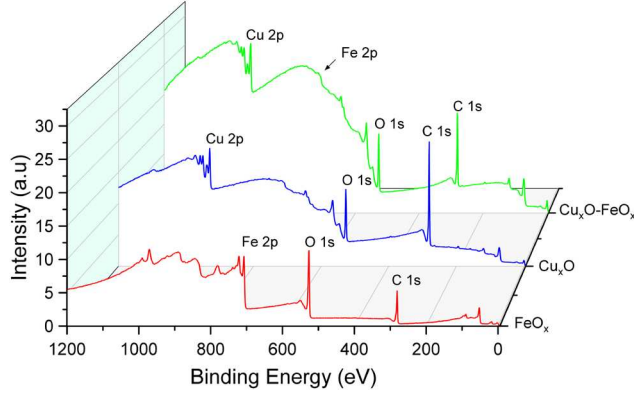
Figure 5: XPS survey of FeOx, CuxO and CuxO-FeOx sputtered on PET.

The proportions of each constituting elements are determined by the area under each peak and reported in Table 1. The major contribution in all films is from carbon and is attributed to the polyethylene substrate. Oxygen is the second most abundant element, followed by copper and iron. To a lesser extent, the presence of carbon and oxygen could also originate from surface impurities since all sample were kept in air. Nitrogen appears as traces only.

Table 1: Surface atomic percentages of the sputtered thin films.

Film/Atomic Composition	Carbon	Oxygen	Copper	Iron	Nitrogen
FeO_x	48.69%	46.40%	-	4.91%	-
Cu_xO	80.80%	16.98%	1.89%	-	0.33%
Cu_xO/FeO_x	71.75%	22.10%	4.90%	1.25%	-

High-resolution XPS spectra were acquired and analyzed using standard calculation from [36]. This refined analysis of the XPS signals for Carbon, Oxygen, Iron and Copper (see SI) informs us about the binding affinity and oxidation state of each of these elements. In all three films, both the

high-resolution analysis of Carbon and Oxygen, indicates that PET substrate shows a high affinity to Oxygen through the presence of C-O single and double bounds (see SI Fig 6-15). Oxygen uptake by PET is a direct consequence of the film's pre-treatment by surface plasma [29].

For the Cu_xO-PET sputtered film, after subtracting all oxygen that are bound to C1s, we are left with 1.21% of oxygen atoms that can be linked to the actual copper atoms. The ratio Cu:O is thus close to 1:1 implying that the metal layer is composed primarily of CuO [37]. It is worth to note the lack of carbon to metal bonding peak (SI Fig 7), which implies that oxygen might be the main (if not the only) bridge between the metallic film and the substrate.

For the FeO_x-PET sputtered films, while the carbon composition (SI Fig 9) is comparable to the one observed for the Cu_xO-PET sample, calculations for oxygen indicates that 33.4% of oxygen is bound to other than carbon. With an overall 4.91% of iron, all of the remaining oxygen is not expected to bind the metal and most probably corresponds to surface contamination. Iron analysis (SI Fig 11) shows a typical $p_{3/2}$ multiplet suggesting the presence of Fe_2O_3. The lack of additional Fe(0) splitting of the p bands implies that we do not have any significant FeO [38].The presence of Fe_2O_3 (or higher complexes) explains in part the relatively high oxygen content mentioned previously. With respect to the high-resolution oxygen analysis, the binding energies that correspond to the different state of iron (e.g. O-Fe(II) and O-Fe(III)) are, however, too close to each other (529.9 and 530.0 eV) to be clearly differentiated (see SI Fig 10)[39]. Here again, the lack of carbon to metal bonding peak, in the high-resolution carbon analysis (see SI Fig 9), implies that oxygen might be the main (if not the only) bridge between the metallic film and the substrate.

For the Cu_xO-FeO_x-PET cosputtered film, by subtracting all oxygen that are bound to carbon using the C 1s spectra calculation method, we are left with 7.6% of oxygen atoms that can be

linked to the present metals. It follows that the ratio of oxygen to metal (Cu and Fe combined) is about 1.2:1. The intense oxygen-bound-to-metal band, in the high-resolution oxygen $1s$ spectra (SI Fig 13), reflects a higher metal content. The high resolution copper spectra is marked by well-defined doublet around 930 eV (SI fig 14), which indicates a mixture of oxidation states; possibly Cu(II) and Cu^0. The presence of Cu^0 could explain the presence of the auger satellite bands. The origin of these bands is unclear and could be a result of Fe/O interactions. The high-resolution iron spectrum (SI fig 15) is marked by little structure and a considerable amount of noise that is attributed to the small quantity of iron present.

3.2.2. Steady-state spectroscopy

The sputtered metal oxides absorption spectra are shown in Figure 6 (with signal from the bare polyethylene substrate being subtracted). Given the stark difference in absorbance between the three films, the difference in efficiency reported in Figure 2 can be explained at first sight as follow: the higher the absorbance, the higher the probability to generated ions and other ROS [29].
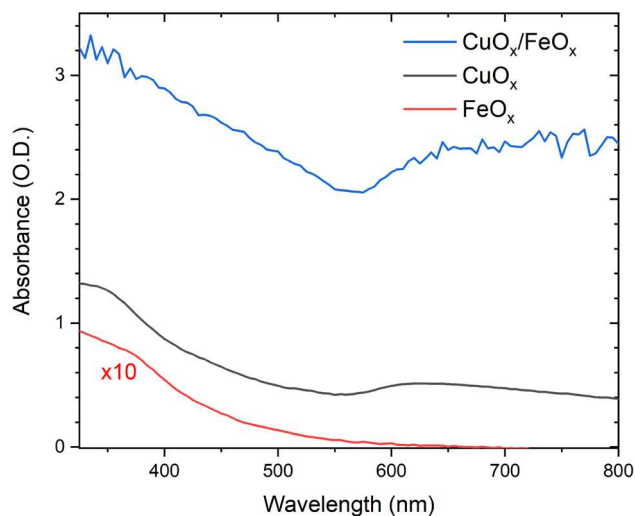
Figure 6: UV-Vis spectrum for the FeO$_x$, Cu$_x$O and mixed Cu$_x$O/FeO$_x$ thin film. The background was set by subtracting the polyethylene substrate. Note that the spectra for FeO$_x$ was multiplied by a factor of 10.

The spectra of the thin films are comprised of a multitude of broad and overlapping absorbance bands that are difficult to assign to specific transitions. In the case of transition metal oxides, we are expecting three types of contributions in the visible region [40]: (i) ligand to metal charge transfer (LMCT) between the oxygen *2p* and the metal *3d* orbitals, (ii) simultaneous pair electronic (SPE) excitation between magnetically coupled metal centres, and (iii) the iron's indirect ligand field (LF) *d-d* transitions. While, the MLCT and SPE are expected to occur in the near UV region, the absorption tails that spams the visible region above 500 nm are generally attributed to various LF transitions [41, 42].

Using the Tauc plot approximation [43] to evaluate the maximum band gap energy for each of the sputtered thin films (see SI Fig x), we found that both FeO$_x$ and Cu$_x$O have a band gap bellow 2.9 eV (>425 nm), while the mixed Cu$_x$O/FeO$_x$ thin film has a band gap bellow 2.3 eV (>540 nm). Interestingly, the estimated band-gaps show that the interaction between Fe- and Cu-oxides, in the composite film, lowers the band-gap. Consequently, effective charge separation, in the composite film, takes place under illumination up to ~540 nm (compared to ~425 nm for pure Fe- and Cu-oxides). This increase in spectral-range activity is expected to result in higher efficiency of ROS generation and ion liberation, as discussed subsequently.

Semiconductors usually present both direct and indirect inter-band transitions. The direct band gap is common on thin films, whereas indirect band-gap transitions are generally found for relatively thick films [44]. The absorption between 600-800 nm in the Cu$_x$O and the FeO$_x$-Cu$_x$O

films is attributed to the intrinsic d-d transition induced in the Cu_xO oxide [40, 45]. The weak absorption at 500-600 nm reflects the absence of the contribution of the inter-band transition of Cu_2O-species [11, 26].

3.2.3. Energy dispersive X-ray spectroscopy

The energy dispersive X-ray spectroscopy (EDS) of the Cu_xO-FeO_x-PET sputtered film is shown in Figure 7. The atomic mapping shows a homogeneous distribution of the Fe-, Cu- and O-content. The density of Cu-atoms seems higher than that of the Fe-atoms, in agreement with the XPS survey analysis (Table 1). This density difference can be attributed to the high deposition rate of Cu when using HiPIMS compared to conventional magnetron sputtering methods used for Fe [46]. It has been reported that denser films were obtained by HiPIMS with minimal ions/particulates release compared to DCMS [11, 47]. The mapping of O, Cu and Fe atoms shows a homogeneous distribution, which confirms that all elements are well mixed (no major Cu_xO or FeO_x domains).
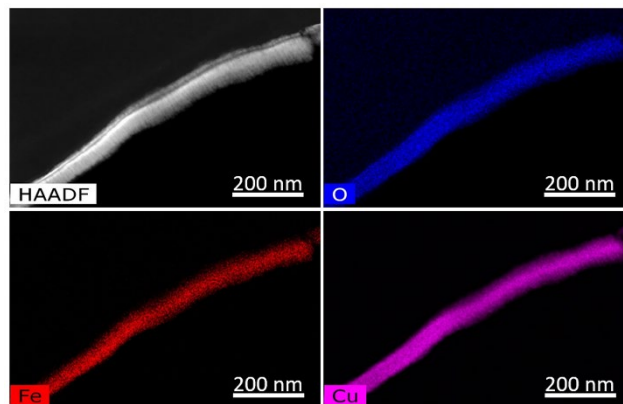
Figure 7: Energy dispersive X-ray spectroscopy of the Cu_xO-FeO_x-PET sputtered film. Scale bar is 200 nm. The corresponding energy dispersive X-ray spectra is shown in SI Fig 5.

3.3. Photo-electron dynamics of Cu_xO, FeO_x and Cu_xO-FeO_x thin films

3.3.1. In sputtered Cu_xO-PET films

The ultrafast dynamics of the films are investigated by means of pump-probe spectroscopy. The 400 nm pump mimics the exposure to UV light and the subsequent electronic and nuclear dynamics are monitored in the whole visible region with a femtosecond resolution up to a couple of nanoseconds. Figure 8 shows the dynamics of the Cu_xO-PET sputtered film as a series of difference spectra at selected time delays. We first note that the superimposed oscillatory patterns in the 650-800 nm region are an artefact of the white light probe pulse.
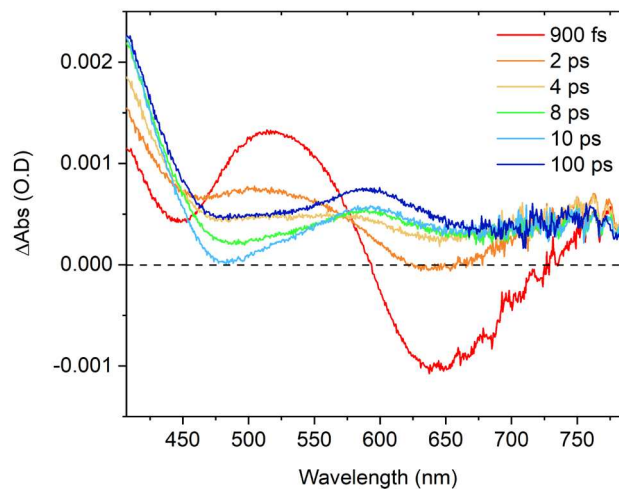
Figure 8: Transient absorption spectra of the Cu_xO thin film as a function of wavelength at 1mW excitation at 400 nm.

Given the electronic nature of the sputtered thin films, the above band-gap 400 nm excitation produces an immediate range of electrons and holes (within the ~100 fs of the excitation pulse) [48, 49]. Shortly after excitation, the excited electrons exhibit a relaxation and reach the lowest energy levels in the conduction band. This decrease in energy gap is expected to occur within the

first hundreds of femtoseconds and is accompanied with a red shift of the transient signal features [48, 49]. It has been reported that other early electronic relaxation mechanisms can contribute to the transient signal, such as band filling and band gap shrinkage, however, they are expected to occurs on the hundreds of femtosecond time scales [50]. All of these relaxation process falls within the limits of our time resolution. After ultrafast relaxation of the generated hot electron and hole pairs, Figure 9 illustrates the four major electronic phenomena that are contributing to our signal.
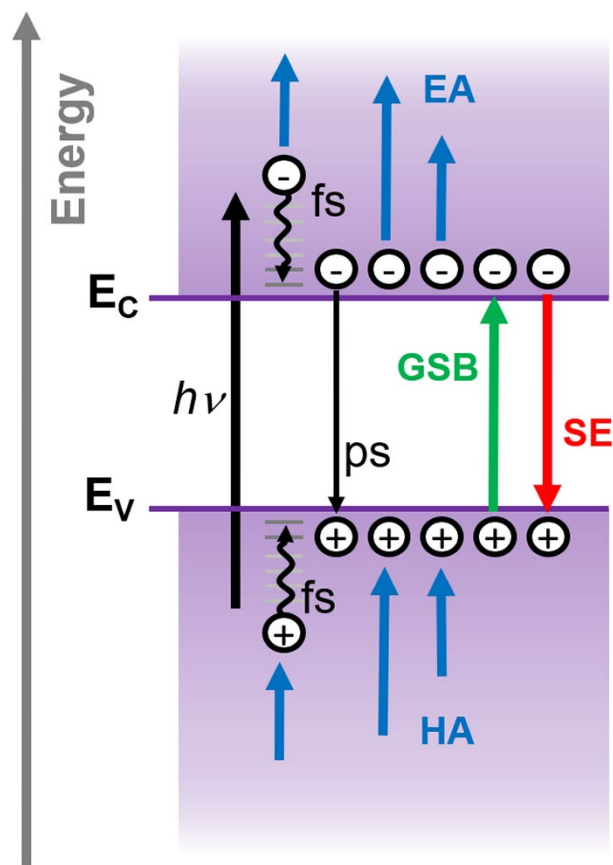
Figure 9: Scheme of the different photo-induced processes and their contribution to the transient signal. Are considered: the pulse-limited (hv) electron-hole separation, femtosecond hot electron and hole relaxation (fs) and picosecond charge recombination (ps). The signal contributions are:

ground state bleach (GSB) and stimulated emission (SE), excited state electron absorption (EA) and hole absorption (HA).

The positive signals are expected to originate from (*i*) transitions from the valence band into the photogenerated holes, called hole absorption (HA), or from (*ii*) transition from the photo-excited electrons in trapped states to higher levels in the conduction band, called electron absorption (EA). The positive signal thus corresponds to a combination of HA and EA. On the other hand, negative transient signals are representative of either (iii) ground state bleach (GSB) or (iv) stimulated emission (SE). The negative features at early time delays, peaking at ~650 nm, reflect the broad absorption band, which peak at ~630 nm in the steady state absorbance spectrum. This transient negative band is thus primarily assigned to GSB. The apparent shift of transient signal with respect to the absorbance spectra can be attributed to SE, which corresponds to the induced transitions of the relaxed electrons back into the valence band.

The transient data is comprised of exponentially evolving spectral bands on top of which sits a time-dependent oscillation. While overlooking the oscillation (present in the first ~100 ps), in a first instance, the data is globally fitted by means of singular value decomposition (SVD). The data can be satisfactorily fitted with a bi-exponential function of decay time 1.2 ps and a non-decaying component. The global analysis results in the decay associated spectra (DAS) shown in *Figure 10*.
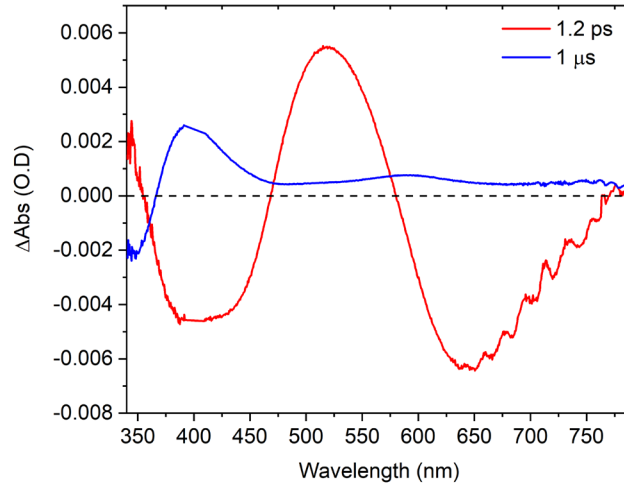
Figure 10: Decay associated spectra (DAS) of Cu$_x$O after satisfactory bi-exponential fitting via SVD.

Each component in the DAS corresponds to the spectral evolution associated to a specific exponential decay. The fact that a unique 1.2 ps time constant can satisfactorily describe the fast dynamics across our visible window indicates that all contributing EA, HA, GSB and SE occurs in the same timescale. In particular, the positive feature peaking at ~520 nm, which corresponds to the decay of both EA and HA, indicates that charge recombination time between photo-generated holes and electrons takes place in 1.2 ps. Similar time constant (3 ps) have been deduced for charge recombination in hematite while being excited at similar wavelength [48]. Additionally, a similar 1–2 ps decay component was monitored in graphene oxide and attributed to electron trapping by shallow defect sites [28, 51]. Accordingly, the non-decaying signal is ascribed to trapped electronic states, similar to the one monitored in hematite [48]. It is indeed possible that our metal oxides have low-lying electronic states below the conduction band edge [52], as well as oxygen-deficient sites [53].

The negative transient signal below 370 nm in the non-decaying DAS component (Figure 10) indicates a lack of excited state absorption. The lack of substantial HA and EA contributions in this spectral region indicates that no transient transitions are readily available at these energies, from either the valence or the conduction bands. In particular, the negative signal indicates that photo-excited electrons cannot access energies above that level. Consequently, the sharp edge in the non-decaying DAS component at ~370 nm points to the upper limit of the conduction band, with a value of 3.4 eV above the band gap, similar to that monitored in hematite [49].
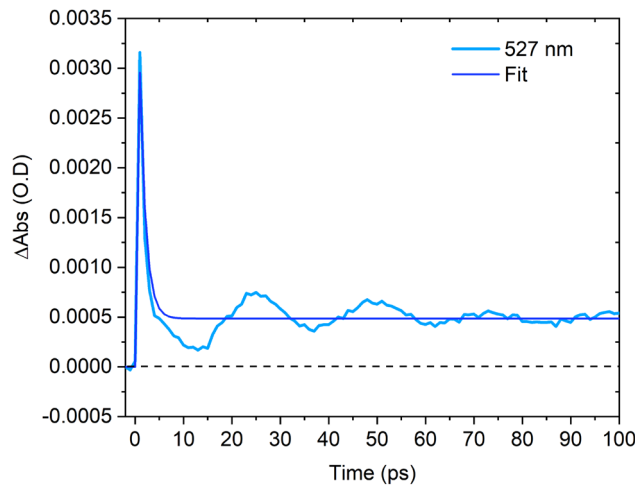
Figure 11: Kinetic profile for the Cu$_x$O thin film for probe wavelength 527 nm and its exponential fit.

The monitored oscillations, as shown in Figure 11 were extracted from the original data set by subtracting the SVD fit. The residual 2D-matrix and details of the procedure can be found in SI. The period of oscillations as well as its relative amplitude, with respect of the total transient signal amplitude, is unaffected by the pump power and is thus intrinsic to the metallic film. The time dependent, t, oscillatory signal is modelled, for each wavelength (λ) as a single damped sine wave following equation:

$$\Delta A(\lambda) = ae^{-t/\tau}\sin(2\pi t/f + \varphi)$$

where a is the amplitude, τ is the time constant of the envelope (damping), f is the frequency and φ the phase of the oscillation. A sample of this fitting is illustrated in Figure 12.
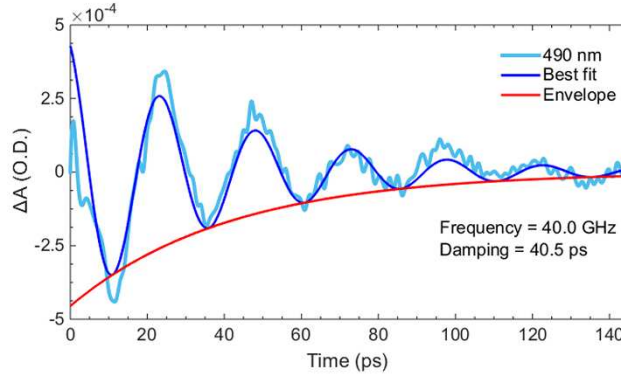
Figure 12: Residual (data – exponential fit) from Cu$_x$O films taken at 490 nm (light blue) and its best fit (dark blue, smooth). The exponential envelope is added as a guide (red).

Over the range from 440 to 560 nm, where the oscillation is predominant, the mean frequency of the oscillations is about 40.0 GHz. Such frequency matches that of a longitudinal acoustic phonon, similar to the ones monitored in various metal oxides thin films [48, 54, 55]. Furthermore, the phase of oscillation is constant across the visible region, as expected for phonons [56]. Acoustic phonons are generated by the excitation pulse as it initially creates holes and hot electrons [57]. These hot electrons and holes collide with the lattice, thus locally increasing the temperature. Thermal expansion of the excited region then results in elastic deformations that modify the material's refractive index. The probe pulse is consequently modulated by the moving compressional wave. The existence of photo-induced acoustic phonons implies a strong coupling between the electronic and lattice effects [48]. Additionally, the longevity of the phonon, which has a damping of 40.5 ps, alludes to the plasticity of the material. The frequency of these

24

oscillations corresponds to the ones monitored in vanadium oxides thin films while in their metallic phases. It was in fact shown that insulating character of vanadium oxides are marked by frequencies bellow 10 GHz [55]. By analogy, the present 40.0 GHz in Cu_xO could be a marker of its metallic character. It was also demonstrated that the phonon frequency, damping coefficient and amplitude are modulated to a lesser extent by the thin film thickness [54].

3.3.2. In sputtered FeO$_x$-PET films
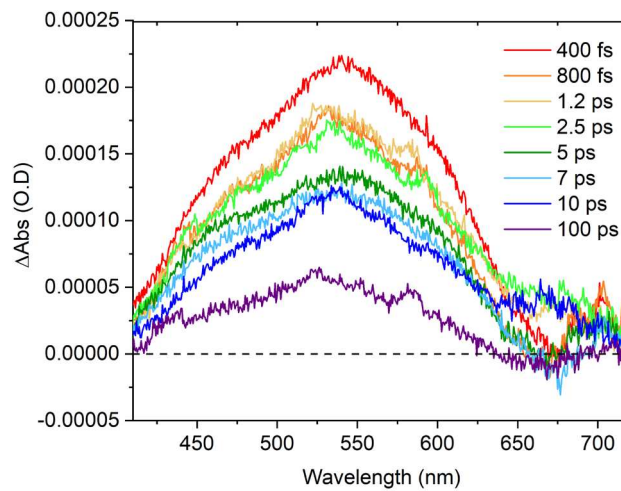
Figure 13: Transient absorption spectra of the FeO$_x$ thin film at selected time delays, under 3.5 mW excitation at 400 nm.

Figure 13 shows the transient difference spectra of the FeO_x thin film at different time delays. Broad and positive bands that peaks around the band gap energy mark both short and longer time delays. Similarly, to the Cu_xO results, positive features indicate that the signals are dominated by a combination of EA and HA. The lack of substantial spectral shifts of the positive features, as expected from the relaxation of hot electrons and holes, indicates that these processes take place within the first few hundreds of femtoseconds. It is in fact reported that in the case of hematite, a structurally similar semiconductor, these processes occur with a time constant of ~250 fs. The

transient signals are analyzed by means of SVD. The data can be satisfactorily fitted with a bi-exponential function with lifetime values of 9.7 ps and 5 ns. Note that no oscillatory features are monitored in this sample (see kinetic in SI Fig 21). The lack of oscillatory signal indicates an apparent decoupling between the lattice and the photo-generated hot electrons.
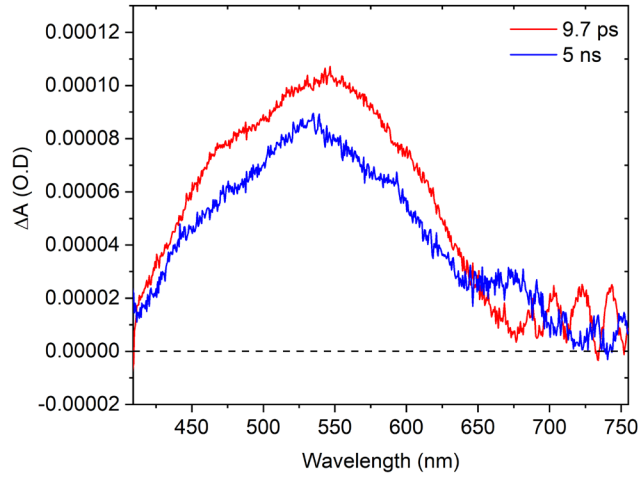
Figure 14: DAS of FeO$_x$ film after satisfactory bi-exponential fitting via SVD.

The resulting DAS shows similar spectral features for both components, represented in Figure 14. In comparison to the sputtered Cu$_x$O thin film, the 9.7 ps component is assigned to slower electron-holes recombination, as expected if there is limited coupling between the hot electrons and the lattice. The 5 ns component corresponds to less stable trapped electron-hole pairs compared to the Cu$_x$O thin film. The FeO$_x$ results also differs from that of hematite by the lack of clear negative features adjacent to the main positive band [49]. On one hand, the absence of negative signal above the band gap (400-530 nm) indicates either a stronger participation of HA to the signal, or that the conduction band is wider compared to that of hematite, up to 3 eV above the bandgap. On the other hand, the absence of negative features at energies bellow the band gap (> 620 nm) indicates that the conduction band is continuous within the first 1.6 eV.

3.3.3. In sputtered Cu_xO-FeO_x-PET films
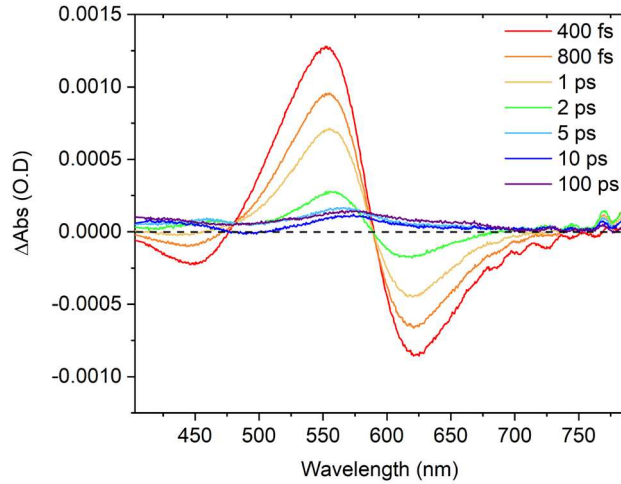
Figure 15: Transient absorption spectra of the Cu_xO/FeO_x thin film at selected time delays, under 3.5 mW excitation at 400 nm.

Selected transient difference spectra at different time delays are shown in Figure 15 for the mixed Cu_xO-FeO_x thin film. The spectral features of the GSB is expected to mimic that of the sample's absorbance. In this case, however, the sharp negative signal at ~620 nm peaks at wavelength where the absorbance of the sample is minimal. On one hand, this discrepancy indicates that the expected (negative) GSB is overcome by strong (positive) HA and EA signals at both early and later time delays. On the other hand, the fact that the negative signal peaks at higher wavelength (lower energies) than expected indicates that it is most probably due to SE from the photo-excited electrons.
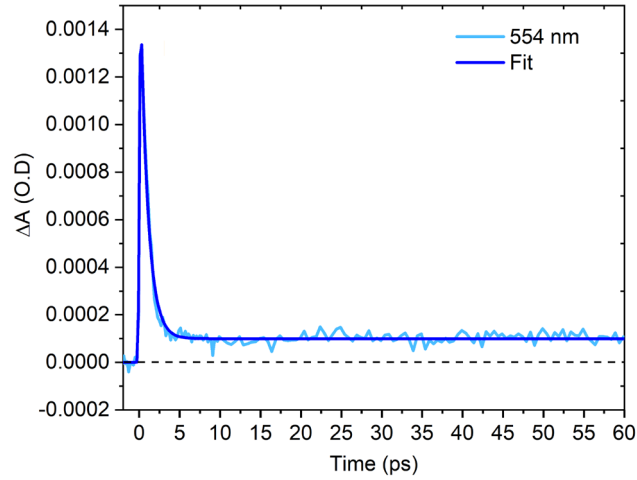
Figure 16: Kinetic trace of the Cu_xO/FeO_x thin film at 554 nm and its exponential fit.

Global analysis was also performed by means of SVD, thus overlooking in the first place the weak oscillatory signal that can be seen in the kinetic traces (Figure 16). The data were satisfactorily fitted with a bi-exponential function with lifetimes of 900 fs and 11 ns. Note that given our restricted time window, the 11 ns is to be understood as a non-decaying component. The resulting DAS is shown in Figure 17.
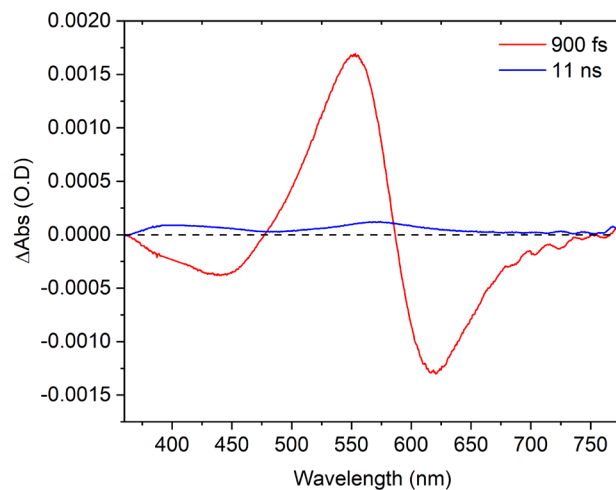
Figure 17: DAS from Cu_xO/FeO_x film after satisfactory bi-exponential fitting via SVD.

As noted previously the relaxation mechanisms of the photogenerated hot electrons and holes are expected to occur within the first hundreds of femtoseconds. Similarly to the case of Cu_xO and FeO_x, the fact that the entire region can be satisfactorily fitted with the same 900 fs indicates that this time constant corresponds to the electron-hole recombination. The longest 11 ns component is again associated with trapped electronic states [48] or with possible intra-gap states generated by the coupling of the two metal oxides. This 11 ns DAS component is characterized by a continuous and featureless positive signal that spam the entire spectral window. This long living signal thus resembles that of the Cu_xO and indicates that the conduction band has no apparent discontinuity, at least up to 3.4eV above the bandgap (in comparison to the previous Cu_xO film or to hematite which has a gap in the conduction band [49]).
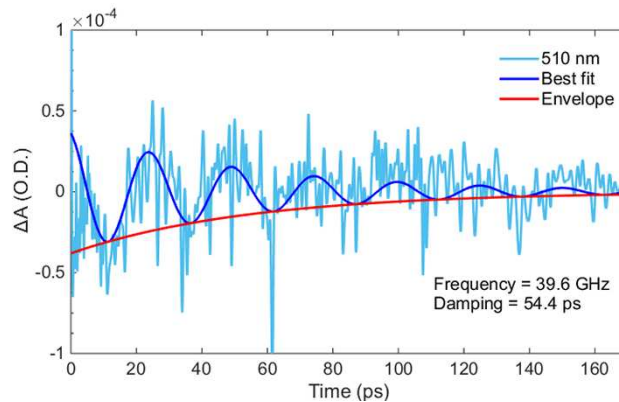
Figure 18: Residual (data – exponential fit) from Cu_xO/FeO_x film taken at 510 nm (light blue) and its best fit (dark blue). The exponential envelope is added as a guide (red).

The weak oscillatory pattern that can be seen in Figure 16 reminds that of the phonon monitored for the sputtered Cu_xO. Similarly, the oscillations in the Cu_xO-FeO_x sample are extracted from the original data set by subtracting the SVD fit. The residual matrix is treated as previously described. Sample of residual fitting is shown in Figure 18. Over the range from 460 to 550nm, the maximum

oscillation amplitude is found at 510 nm, the mean frequency of the oscillations and average-damping constant are found to be 39.6 GHz and 54.6 ps, respectively. While the oscillation's frequency and damping are similar to that of the Cu_xO film, the relative amplitude is much lower while compared to the sputtered Cu_xO-FeO_x samples. While the data is marked by a fast electron-hole recombination (~900 fs), indicative of strong coupling between hot electrons and the lattice, the reduced amplitude of oscillations is certainly a reflection of an homogeneous distribution of both Cu and Fe atoms (i.e. no large Cu_xO domains) across the film, as evidenced by the EDS mapping (Figure 7).

When comparing all three samples, even if their ultrafast (fs-ps-ns) inspection indicates clear differences in electron dynamics and electronic structures, in the physiological time frame (μs-ms), all these differences are leveled: All three samples exhibit a ns-long living broad and positive signal associated to trapped charge separated states. It is then sensical to imagine that it is these high energy electrons that lead to the formation of harmful ions and other ROS, which, along with the released ions, ultimately confer the films their antibacterial properties.

Conclusion

The photocatalytic efficiency of the Fe, Cu and mixed FeCu oxides thin films was demonstrated on colonies of E-coli. Full inactivation under inddor light was obtained in matters of hours only. By achieving total bacterial inactivation within 60 min, the composite film is twice and trice faster than Cu_xO and FeO_x films, respectively. Cytometry measurements show at least two distinct (external and internal) mechanisms for bacterial inactivation. MDA quantification suggests that oxidative stresses at the interface between the film and the organisms are the main driving forces

leading to bacterial inactivation. the internal effect of the generated ions, after uptake by the organism, seems to be minimal. In terms of structure, all three films show a homogeneous distribution of their constitutive elements, but each having distinct metallic oxidation states, as evidenced by energy dispersive X-ray, X-ray photo electron and optical spectroscopic analysis. While the films are structurally distinct to one-another, ultrafast time-resolved spectroscopy reveals that in all three films, the major oxidative stresses and minor ions release are a direct consequence of long-lived (>ns) photo-generated electron-hole pairs within the metallic layer. Given the stark difference in absorbance between the three films and difference in band-gap energy, the difference in efficiency can be explained as follow. The interaction between Fe- and Cu-oxides in the composite film confers the film (1) higher absorption and (2) enhance its reactivity by lowering its band-bap energy. Both effects are expected to result in a higher number of long-lived photo-generated electron-hole pair; the higher the number of long-lived electron-hole pair, the higher the probability to generated ions and other ROS. It is important to mention that the antibacterial thin film here studied are composed solely of non-toxic and earth abundant metals, deposited on stress resistant PET. Consequently, the present study opens the door for potential industrial application of these coatings on polymer surfaces in various health-related products.

ASSOCIATED CONTENT

Supporting Information.

The following file is available free of charge.

Supplementary material, which includes details of the Tauc plots, X-ray analysis and oscillation

analysis (PDF)

AUTHOR INFORMATION

Corresponding Author

* Corresponding authors: a.chauvet@sheffield.ac.uk and sami.rtimi@epfl.ch , Tel: +41216936150.

Author Contributions

The manuscript was written through contributions of all authors. All authors have given approval to the final version of the manuscript.

Funding Sources

ABBREVIATIONS

Cu_xO, copper oxides; DAS, decay associated spectra; DCMS, direct current magnetron sputtering; DRS, diffuse reflectance spectroscopy; EA, excited state electron absorption; EDS, energy dispersive X-ray spectroscopy; FeO_x, iron oxide; GSB, ground state bleach; HA, hole absorption; HiPIMS, high power impulse magnetron sputtering; ICP-MS, inductively coupled plasma mass spectrometry; LF, ligand field; LMCT, ligand to metal charge transfer; MDA, 3,4-Methylenedioxyamphetamine; PET, polyethylene; ROS, reactive oxygen species; SE, stimulated emission; SOD, superoxide dismutase; SPE, simultaneous pair electronic; SVD, singular value decomposition; TEM, transmission electron microscopy; XPS, X-ray photoelectron spectroscopy.

REFERENCES

[1] United Nations. https://www.un.org/sustainabledevelopment/sustainable-development-goals/.

[2] World Health Organization. https://www.who.int/antimicrobial-resistance/en/.

[3] *HAI Fact Sheet*; World Health Organization: **2014**.

[4] S. Rtimi, Indoor Light Enhanced Photocatalytic Ultra-Thin Films on Flexible Non-Heat Resistant Substrates Reducing Bacterial Infection Risks. *Catalysts* **2017,** *7* (2), 57.

[5] S. Rtimi, C. Pulgarin, M. Robyr, A. Aybush, I. Shelaev, F. Gostev, V. Nadtochenko and J. Kiwi, Insight into the Catalyst/Photocatalyst Microstructure Presenting the Same Composition but Leading to a Variance in Bacterial Reduction under Indoor Visible Light. *Applied Catalysis B: Environmental* **2017,** *208*, 135-147.

[6] H. Wang, H. Tong, H. Liu, Y. Wang, R. Wang, H. Gao, P. Yu, Y. Lv, S. Chen, G. Wang, M. Liu, Y. Li, K. Yu and C. Wang, Effectiveness of Antimicrobial-Coated Central Venous Catheters for Preventing Catheter-Related Blood-Stream Infections with the Implementation of Bundles: a Systematic Review and Network Meta-Analysis. *Annals of Intensive Care* **2018,** *8* (1), 71.

[7] N. M. Lai, N. Chaiyakunapruk, N. A. Lai, E. O'Riordan, W. S. C. Pau and S. Saint, Catheter Impregnation, Coating or Bonding for Reducing Central Venous Catheter-Related Infections in Adults. *Cochrane Database of Systematic Reviews* **2016,** (3).

[8] S. Rtimi, S. Giannakis, M. Bensimon, C. Pulgarin, R. Sanjines and J. Kiwi, Supported TiO$_2$ Films Deposited at Different Energies: Implications of the Surface Compactness on the Catalytic Kinetics. *Applied Catalysis B: Environmental* **2016,** *191*, 42-52.

[9] S. Rtimi, O. Baghriche, C. Pulgarin, A. Ehiasarian, R. Bandorf and J. Kiwi, Comparison of HIPIMS Sputtered Ag- and Cu-Surfaces Leading to Accelerated Bacterial Inactivation in the Dark. *Surface and Coatings Technology* **2014,** *250*, 14-20.

[10] S. Rtimi, D. D. Dionysiou, S. C. Pillai and J. Kiwi, Advances in Catalytic/Photocatalytic Bacterial Inactivation by Nano Ag and Cu Coated Surfaces and Medical Devices. *Applied Catalysis B: Environmental* **2019,** *240*, 291-318.

[11] S. Rtimi, S. Konstantinidis, N. Britun, M. Bensimon, I. Khmel and V. Nadtochenko, Extracellular Bacterial Inactivation Proceeding Without Cu-Ion Release: Drastic Effects of the Applied Plasma Energy on the Performance of the Cu-Polyester (PES) Samples. *Applied Catalysis B: Environmental* **2018,** *239*, 245-253.

[12] A. Alhussein, S. Achache, R. Deturche, F. Sanchette, C. Pulgarin, J. Kiwi and S. Rtimi, Beneficial Effect of Cu on Ti-Nb-Ta-Zr Sputtered Uniform/Adhesive Gum Films Accelerating Bacterial Inactivation under Indoor Visible Light. *Colloids and Surfaces B: Biointerfaces* **2017,** *152*, 152-158.

[13] S. J. Dancer, The role of Environmental Cleaning in the Control of Hospital-Acquired Infection. *Journal of Hospital Infection* **2009,** *73* (4), 378-385.

[14] A. Kramer, I. Schwebke and G. Kampf, How Long do Nosocomial Pathogens Persist on Inanimate Surfaces? A Systematic Review. *BMC Infectious Diseases* **2006,** *6* (1), 130.

[15] K. Keyer and J. A. Imlay, Superoxide Accelerates DNA Damage by Elevating Free-Iron Levels. *Proceedings of the National Academy of Sciences* **1996,** *93* (24), 13635.

[16] R. Bauer, G. Waldner, H. Fallmann, S. Hager, M. Klare, T. Krutzler, S. Malato and P. Maletzky, The Photo-Fenton Reaction and the TiO_2/UV Process for Waste Water Treatment − Novel Developments. *Catalysis Today* **1999,** *53* (1), 131-144.

[17] J. Ndounla, D. Spuhler, S. Kenfack, J. Wéthé and C. Pulgarin, Inactivation by Solar Photo-Fenton in PET Bottles of Wild Enteric Bacteria of Natural Well Water: Absence of Re-Growth after One Week of Subsequent Storage. *Applied Catalysis B: Environmental* **2013,** *129*, 309-317.

[18] C. Ruales-Lonfat, N. Benítez, A. Sienkiewicz and C. Pulgarín, Deleterious Effect of Homogeneous and Heterogeneous Near-Neutral Photo-Fenton System on *Escherichia coli*. Comparison with Photo-Catalytic Action of TiO_2 During Cell Envelope Disruption. *Applied Catalysis B: Environmental* **2014,** *160-161*, 286-297.

[19] J. Kiwi and S. Rtimi, Mechanisms of the Antibacterial Effects of TiO_2–FeO_x under Solar or Visible Light: Schottky Barriers versus Surface Plasmon Resonance. *Coatings* **2018,** *8* (11), 391.

[20] M. R. Dhananjeyan, E. Mielczarski, K. R. Thampi, P. Buffat, M. Bensimon, A. Kulik, J. Mielczarski and J. Kiwi, Photodynamics and Surface Characterization of TiO_2 and Fe_2O_3 Photocatalysts Immobilized on Modified Polyethylene Films. *The Journal of Physical Chemistry B* **2001,** *105* (48), 12046-12055.

[21] M. R. Dhananjeyan, J. Kiwi and K. R. Thampi, Photocatalytic Performance of TiO and FeO Immobilized on Derivatized Polymer Films for Mineralisation of Pollutants. *Chemical Communications* **2000,** (15), 1443-1444.

[22] J. Fernandez, J. Bandara, A. Lopez, P. Buffat and J. Kiwi, Photoassisted Fenton Degradation of Nonbiodegradable Azo Dye (Orange II) in Fe-Free Solutions Mediated by Cation Transfer Membranes. *Langmuir* **1999,** *15* (1), 185-192.

[23] D. Quaranta, T. Krans, C. E. Santo, C. G. Elowsky, D. W. Domaille, C. J. Chang and G. Grass, Mechanisms of Contact-Mediated Killing of Yeast Cells on Dry Metallic Copper Surfaces. *Applied and Environmental Microbiology* **2011,** *77* (2), 416.

[24] C. E. Santo, E. W. Lam, C. G. Elowsky, D. Quaranta, D. W. Domaille, C. J. Chang and G. Grass, Bacterial Killing by Dry Metallic Copper Surfaces. *Applied and Environmental Microbiology* **2011,** *77* (3), 794.

[25] X. Qiu, M. Miyauchi, K. Sunada, M. Minoshima, M. Liu, Y. Lu, D. Li, Y. Shimodaira, Y. Hosogi, Y. Kuroda and K. Hashimoto, Hybrid Cu_xO/TiO_2 Nanocomposites as Risk-Reduction Materials in Indoor Environments. *ACS Nano* **2012,** *6* (2), 1609-1618.

[26] S. Rtimi, R. Sanjines, C. Pulgarin and J. Kiwi, Effect of Light and Oxygen on Repetitive Bacterial Inactivation on Uniform, Adhesive, Robust and Stable Cu-Polyester Surfaces. In *Journal of Advanced Oxidation Technologies*, **2017**; Vol. 20.

[27] S. Rtimi, V. Nadtochenko, I. Khmel, M. Bensimon and J. Kiwi, First Unambiguous Evidence for Distinct Ionic and Surface-Contact Effects During Photocatalytic Bacterial Inactivation on Cu–Ag Films: Kinetics, Mechanism and Energetics. *Materials Today Chemistry* **2017,** *6*, 62-74.

[28] S. Rtimi, C. Pulgarin, R. Sanjines and J. Kiwi, Novel FeO_x–Polyethylene Transparent Films: Synthesis and Mechanism of Surface Regeneration. *RSC Advances* **2015,** *5* (98), 80203-80211.

[29] S. Rtimi and J. Kiwi, Bactericide Effects of Transparent Polyethylene Photocatalytic Films Coated by Oxides under Visible Light. *Applied Catalysis B: Environmental* **2017,** *213*, 62-73.

[30] T. U. o. Sheffield The Lord Porter Ultrafast Laser Spectroscopy Laboratory. https://www.sheffield.ac.uk/faculty/science/research/facilities/laserlab.

[31] M. K. S. Ballo, S. Rtimi, S. Mancini, J. Kiwi, C. Pulgarin, J. M. Entenza and A. Bizzini, Bactericidal Activity and Mechanism of Action of Copper-Sputtered Flexible Surfaces Against Multidrug-Resistant Pathogens. *Applied Microbiology and Biotechnology* **2016,** *100* (13), 5945-5953.

[32] U. S. Enderlein, R. E. Enderlein and W. P. Williams, Chapter 2 - Water Quality Requirements. In *Water Sanitation and Health* World Health Organization: 2014.

[33] M. Kumar and A. Puri, A Review of Permissible Limits of Drinking Water. *Indian journal of occupational and environmental medicine* **2012,** *16* (1), 40-44.

[34] A. P. Pugsley and C. A. Schnaitman, Outer Membrane Proteins of *Escherichia coli*. VII. Evidence that Bacteriophage-Directed Protein 2 Functions as a Pore. *Journal of Bacteriology* **1978,** *133* (3), 1181-1189.

[35] L. C. Seaver and J. A. Imlay, Alkyl Hydroperoxide Reductase Is the Primary Scavenger of Endogenous Hydrogen Peroxide in *Escherichia coli*. *Journal of Bacteriology* **2001,** *183* (24), 7173.

[36] B. P. Payne, M. C. Biesinger and N. S. McIntyre, X-Ray Photoelectron Spectroscopy Studies of Reactions on Chromium Metal and Chromium Oxide Surfaces. *Journal of Electron Spectroscopy and Related Phenomena* **2011,** *184* (1), 29-37.

[37] G. Beamson and D. Briggs, *High Resolution XPS of Organic Polymers: The Scienta ESCA300 Database*. Wiley: **1992**.

[38] A. P. Grosvenor, B. A. Kobe, M. C. Biesinger and N. S. McIntyre, Investigation of Multiplet Splitting of Fe 2p XPS Spectra and Bonding in Iron Compounds. *Surface and Interface Analysis* **2004,** *36* (12), 1564-1574.

[39] S. Rtimi, M. Robyr, C. Pulgarin, J. C. Lavanchy and J. Kiwi, A New Perspective in the Use of FeO_x-TiO_2 Photocatalytic Films: Indole Degradation in the Absence of Fe-Leaching. *Journal Of Catalysis* **2016,** *342*, 184-192.

[40] M. Barroso, S. R. Pendlebury, A. J. Cowan and J. R. Durrant, Charge Carrier Trapping, Recombination and Transfer in Hematite (α-Fe$_2$O$_3$) Water Splitting Photoanodes. *Chemical Science* **2013,** *4* (7), 2724-2734.

[41] L. A. Marusak, R. Messier and W. B. White, Optical Absorption Spectrum of Hematite, αFe$_2$O$_3$ Near IR to UV. *Journal of Physics and Chemistry of Solids* **1980,** *41* (9), 981-984.

[42] P. Liao and E. A. Carter, Optical Excitations in Hematite (α-Fe2O3) via Embedded Cluster Models: A CASPT2 Study. *The Journal of Physical Chemistry C* **2011,** *115* (42), 20795-20805.

[43] B. D. Viezbicke, S. Patel, B. E. Davis and D. P. Birnie III, Evaluation of the Tauc Method for Optical Absorption Edge Determination: ZnO Thin Films as a Model System. *physica status solidi (b)* **2015,** *252* (8), 1700-1710.

[44] I. G. Lezama, A. Arora, A. Ubaldini, C. Barreteau, E. Giannini, M. Potemski and A. F. Morpurgo, Indirect-to-Direct Band Gap Crossover in Few-Layer MoTe$_2$. *Nano Letters* **2015,** *15* (4), 2336-2342.

[45] G. Mamba, C. Pulgarin, J. Kiwi, M. Bensimon and S. Rtimi, Synchronic Coupling of Cu$_2$O(p)/CuO(n) Semiconductors Leading to Norfloxacin Degradation under Visible Light: Kinetics, Mechanism and Film Surface Properties. *Journal of Catalysis* **2017,** *353*, 133-140.

[46] T. Kubart, M. Aiempanakit, J. Andersson, T. Nyberg, S. Berg and U. Helmersson, Studies of Hysteresis Effect in Reactive HiPIMS Deposition of Oxides. *Surface and Coatings Technology* **2011,** *205*, S303-S306.

[47] S. Rtimi, C. Pulgarin, O. Baghriche and J. Kiwi, Accelerated Bacterial Inactivation Obtained by HIPIMS Sputtering on Low Cost Surfaces with Concomitant Reduction in the Metal/Semiconductor Content. *RSC Advances* **2013,** *3* (32), 13127-13130.

[48] A. G. Joly, J. R. Williams, S. A. Chambers, G. Xiong, W. P. Hess and D. M. Laman, Carrier Dynamics in α-Fe$_2$O$_3$ (0001) Thin Films and Single Crystals Probed by Femtosecond Transient Absorption and Reflectivity. *Journal of Applied Physics* **2006,** *99* (5), 053521.

[49] S. Sorenson, E. Driscoll, S. Haghighat and J. M. Dawlaty, Ultrafast Carrier Dynamics in Hematite Films: The Role of Photoexcited Electrons in the Transient Optical Response. *The Journal of Physical Chemistry C* **2014,** *118* (41), 23621-23626.

[50] B. R. Bennett, R. A. Soref and J. A. D. Alamo, Carrier-Induced Change in Refractive Index of InP, GaAs and InGaAsP. *IEEE Journal of Quantum Electronics* **1990,** *26* (1), 113-122.

[51] S. Murphy and L. Huang, Transient Absorption Microscopy Studies of Energy Relaxation in Graphene Oxide Thin Film. *J Phys Condens Matter* **2013,** *25* (14), 144203.

[52] D. M. Sherman and T. D. Waite, Electronic Spectra of Fe^{3+} Oxides and Oxide Hydroxides in the Near IR to Near UV. *American Mineralogist* **1985,** *70* (11-12), 1262-1269.

[53] C. Leygraf, M. Hendewerk and G. Somorjai, The Preparation and Selected Properties of Mg-doped p-Type Iron Oxide as a Photocathode for the Photoelectrolysis of Water Using Visible Light. *Journal of Solid State Chemistry* **1983,** *48* (3), 357-367.

[54] Y. D. Glinka, S. Babakiray, T. A. Johnson, M. B. Holcomb and D. Lederman, Acoustic Phonon Dynamics in Thin-Films of the Topological Insulator Bi_2Se_3. *Journal of Applied Physics* **2015,** *117*.

[55] E. Abreu, S. N. Gilbert Corder, S. J. Yun, S. Wang, J. G. Ramírez, K. West, J. Zhang, S. Kittiwatanakul, I. K. Schuller, J. Lu, S. A. Wolf, H.-T. Kim, M. Liu and R. D. Averitt, Ultrafast Electron-Lattice Coupling Dynamics in VO_2 and V_2O_3 Thin Films. *Physical Review B* **2017,** *96*.

[56] M. Grossmann, M. Schubert, C. He, D. Brick, E. Scheer, M. Hettich, V. Gusev and T. Dekorsy, Characterization of Thin-Film Adhesion and Phonon Lifetimes in Al/Si Membranes by Picosecond Ultrasonics. *New Journal of Physics* **2017,** *19* (5), 053019.

[57] M. Radzig, O. Koksharova, I. Khmel, V. Ivanov, K. Yorov, J. Kiwi, S. Rtimi, E. Tastekova, A. Aybush and V. Nadtochenko, Femtosecond Spectroscopy of Au Hot-Electron Injection into TiO_2: Evidence for Au/TiO_2 Plasmon Photocatalysis by Bactericidal Au Ions and Related Phenomena. *Nanomaterials (Basel)* **2019,** *9* (2), 217.

Table of Content Graphic / Graphical abstract